Chapter 2
In Situ Characterization of Photocatalytic Activity

The photocatalytic reactions are initiated from the photoinduced electrons and holes on the surfaces of photocatalyst, which further react with water/oxygen to form reactive oxygen species (ROS) with high reactivity including superoxide anion radical ($^{\bullet}O_2^-$), hydrogen peroxide (H_2O_2), singlet oxygen ($^1O_2$), and hydroxyl radical ($^{\bullet}OH$). The determination of ROS formed from the semiconductor-based photocatalysis and the in situ tracking of the formation sites; trajectory and kinetics are essential for understanding the photocatalytic redox mechanism, thus helping to guide the structure design of the photocatalyst. This chapter focuses on the application of fluorescence, infrared, Raman, electron spin resonance (ESR), and surface photovoltage spectroscopies and atomic force microscopy (AFM) to reveal the above process on the surface of the photocatalyst regarding the surface heterogeneity, crystal facet, and molecule conformation. These studies have greatly promoted the design and application of photocatalyst.

2.1 Fluorescence

Fluorescence is one of the most important ways for the identification, quantification, and kinetics evaluation of ROS. Fluorophores including luminol, fluorescein, coumarin, and tetrafluoroborate are commonly used probes for ROS [1]. The dehydrogenation, esterification, and the intramolecular electron transferring may cause the on–off, off–on, or wavelength shift of the fluorescence. Such variation provides specific information about the ROS formation on the surface of photocatalysts.

J. Zhang et al., *Photocatalysis*, Lecture Notes in Chemistry 100,
https://doi.org/10.1007/978-981-13-2113-9_2

2.1.1 Types of Probing Agents for ROS

Hydrogen Peroxide Oxidized luminol, which is 5-amino-2, 3-diaza-1, 4-naphthoquinone, can react with H_2O_2 to generate the excited state of 3-aminophthalate ion, AP* [2]. It is also an active fluoregen to $^{\bullet}O_2^-$. For the exclusive detection of H_2O_2, the luminol solution was added to the reaction mixture, which was then kept in the dark for ca. 30 min to eliminate $^{\bullet}O_2^-$. Then hemoglobin (Hem) as an oxidant is added into the mixture to form fluorescence. A detection limit of about 1 nM can be achieved through this probe. Besides HEM, $K_3Fe(CN)_6$ could also be used as an oxidant to trigger the fluorescence [3]. The application of luminol is mainly restricted in basic system since it could be used only at higher pH (pH > 10).

Lucigenin (bis-*N*-methylacridinium nitrate) is another typical fluorescent probe for both H_2O_2 and $^{\bullet}O_2^-$ [4], which could be operated at moderate pH (pH = 9). A dioxetane can be produced after the oxidation, which decomposes to the excited state of *N*-methyl acridone. Using the detection of H_2O_2 as an example, lucigenin solution was injected into the suspension of TiO_2 after stopping UV irradiation on TiO_2 powder. On the injection, bluish-green fluorescence appeared and decayed in several seconds. The time integral of the fluorescence intensity is proportional to the amount of H_2O_2, which is used to estimate the H_2O_2 concentration with calibrations.

Superoxide Oxygen Anion As mentioned above, luminol is also widely used for probing $^{\bullet}O_2^-$. The detection limit of $^{\bullet}O_2^-$ with luminol chemiluminescence is estimated to be 0.1 nM. As a reference, MCLA (2-methyl-6-(4-methoxyphenyl)-3, 7-dihydroimidazo (1, 2-a) pyrazin-3-one, hydrochloride), a probe for both $^{\bullet}O_2^-$ and $^1O_2$, can be used to confirm the exclusive detection of $^{\bullet}O_2^-$ together with luminol [5]. The priority of MCLA is its applicability to neutral pH system.

Singlet Oxygen Sensor A singlet oxygen sensor green (SOSG) was employed to detect $^1O_2$, which produces an endoperoxide that fluoresces at 528 nm under the excitation at 488 nm [6]. SOSG shows no appreciable response to $^{\bullet}OH$ or $^{\bullet}O_2^-$. However, when it was used under light illumination, significant problems in photosensitized $^1O_2$ generation and photodecomposition were clearly demonstrated. $^1O_2$ generated in air can also be detected with the terrylene diimide (TDI) derivative, which produces fluorescent diepoxide [7].

Hydroxyl Radical Fluorescein derivatives are commonly used for the probing of $^{\bullet}OH$. For example, 3′-(*p*-hydroxyphenyl) fluorescein (HPF) selectively reacts with $^{\bullet}OH$ to form a strongly emissive fluorescein molecule but does not react with the other ROS [8]. Nonfluorescent Amplex Red is also a commonly used probe for $^{\bullet}OH$ and $^{\bullet}O_2^-$, forming the fluorescent product resorufin [9]. Other probes including terephthalic acid and coumarin derivatives were also active to generate the fluorescent product for detecting $^{\bullet}OH$ in solution, which have no absorption at the excitation wavelength for photocatalysts. Different from the detection methods for $^{\bullet}O_2^-$ and H_2O_2, the probe molecules were present during the photocatalytic reaction, and

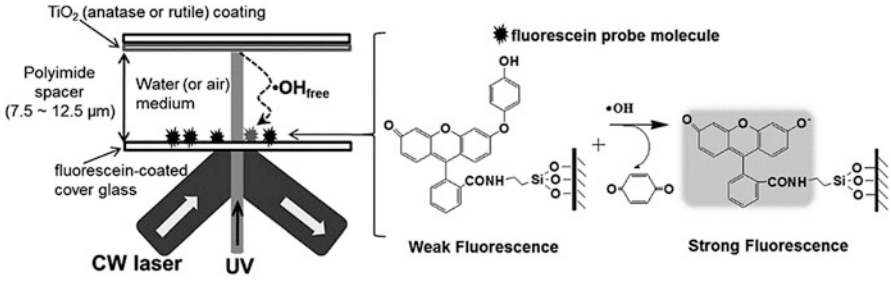

Fig. 2.1 Illustration of the experimental setup for the single-molecule detection of photogenerated •OH in water. Anatase or rutile was coated on the upper cover glass and the modified fluorescein (HPF) was anchored on the lower glass through a silanol group. The intervening gap was controlled using polyimide films. The gap was filled with air-saturated water. (Reproduced from Ref. [10] by permission of John Wiley & Sons Ltd)

after the reaction, the photocatalyst powders were removed from the suspension to improve the precision of the fluorescence spectrophotometry.

2.1.2 Single-Molecule Spectroscopy

Traditional fluorescent spectroscopy provides spectra regarding the intensity, lifetime, and polarization by averaging the emission from trillions of molecules. By contrast, single-molecule fluorescence spectroscopy rests upon the removal of ensemble average, thus allowing the detection of the heterogeneity of the local environment.

Single-molecule spectroscopy can be used to verify the diffusion of •OH from the surface of semiconductor to the solution (Fig. 2.1) [10]. HPF can selectively react with •OH generated on UV-irradiated TiO_2 instead of $O_2^{\bullet-}$, $^1O_2$, and H_2O_2, transforming into a strongly fluorescing product. HPF was anchored on a glass plate through the silanol group and separated from a TiO_2-coated glass plate with a spacer. The distance between the two glass plates was controlled using polyimide films, and the space was filled with air-saturated water. In this way, the generation and the subsequent diffusion of •OH from the illuminated TiO_2 surface to the solution bulk can be directly observed using the single-molecule fluorescence spectroscopy. Interestingly, bright fluorescent signals clearly emerged over the irradiated region of the anatase film after UV irradiation, whereas the signals generated over rutile were negligible. Therefore, the mobile •OH is generated on anatase but not on rutile. The photocatalytic oxidation on rutile is limited to adsorbed substrates whereas that on anatase is more facile and versatile owing to the presence of mobile •OH. This result partly explains the common observations that anatase has higher activity than rutile.

Facet-Selective Photocatalytic Reaction The differences in surface energy levels of the conduction and valence bands, surface structures, and adsorption energies of substrates on the exposed crystal faces may result in face-selective photocatalytic reaction. Fluorescence at the single-molecule and single-particle level has recently evolved as an important tool for studying selective photocatalytic reactions on different facets because of its high sensitivity, simplicity of data collection, and high spatial resolution in microscopic imaging techniques. Several organic dye probes have been successfully employed to detect the generated ROS and identify the active sites on individual TiO_2 nanoparticles by utilizing single-molecule fluorescence spectroscopy. A typical example is from boron dipyrromethene (BODIPY), which has a high extinction coefficient, high fluorescence quantum yield, and good chemical and photostability. It has evolved into versatile fluorescent sensors for biological and chemical detection. On the other hand, the reduction of aromatic nitro compounds to the corresponding hydroxylamines or amines has been widely used as a model system to investigate photocatalytic reduction reactions with semiconductor or metal nanoparticles. The major drawback for the development of a fluorogenic probe based on the reduction of a nitro-substituted benzene moiety for monitoring electron transfer (ET) process lies in the strong quenching effect of nitrobenzene and its reduction products (i.e., phenylhydroxylamine or aniline). Since mono-nitro-substituted BODIPY derivative fails to function as a fluorescent probe, 3, 4-dinitrophenyl modified BODIPY (DN-BODIPY) was designed as a redox-responsive fluorescent probe (Fig. 2.2), where the intramolecular ET process is suppressed when the produced electron-donating group encounters the second nitro group [11]. This probe was applied to both ensemble-averaged and single-molecule fluorescence-monitoring of photoinduced ET process on the TiO_2 surface.

Total internal reflection fluorescence microscopy (TIRFM) was used for monitoring the photocatalytic reduction of DN-BODIPY molecules over single TiO_2 particles. Figure 2.3 A shows typical fluorescence images from a single TiO_2 particle in Ar-saturated methanol containing DN-BODIPY (2 μM) under UV irradiation (middle and right images). A number of fluorescence bursts were generated from individual single particles. The locations of the fluorescence bursts, which were

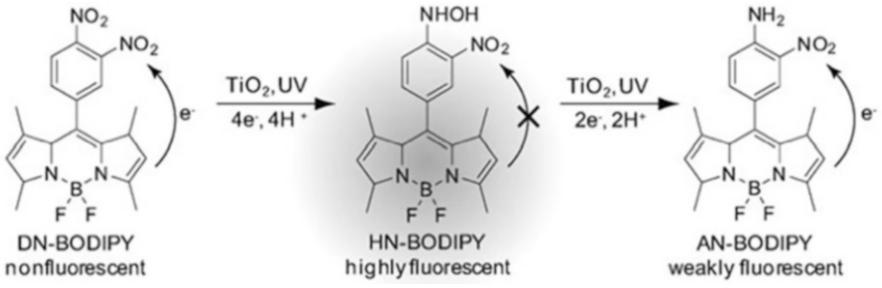

Fig. 2.2 Photocatalytic generation of fluorescent HN-BODIPY from nonfluorescent DN-BODIPY [11]. (Reproduced from Ref. [11] by permission of John Wiley & Sons Ltd)

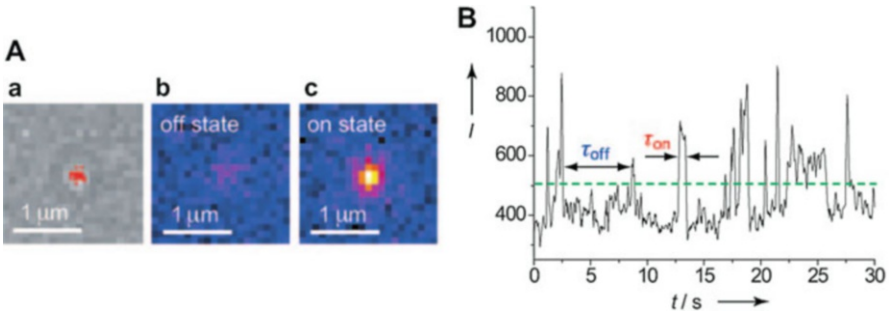

Fig. 2.3 (**a**) Photocatalytic generation of fluorescent HN-BODIPY from nonfluorescent DN-BODIPY. (**a**) Transmission (*a*) of a single TiO_2 particle on the cover glass and fluorescence images (*b* and *c*) of the same particle in Ar-saturated 2.0 mm DN-BODIPY solution under 488 nm laser and UV irradiation (0.5 Wcm^{-2} at the glass surface). The acquisition time of an image was 50 ms. The red dots in the transmission image indicate the location of fluorescence bursts. The accuracy of location was about 50 nm. (**b**) A typical fluorescence intensity trajectory observed for a single TiO_2 particle. The green dashed line indicates the threshold level separating the on and off states. (Reproduced from Ref. [11] by permission of John Wiley & Sons Ltd)

determined by fitting two-dimensional Gaussian functions to the intensity distribution of each fluorescence spot, are likely distributed over the particle according to the red dots in the transmission image. The fluorescence lifetimes of the in situ generated bursts over single TiO_2 particles were measured by combining confocal microscopy with a time-correlated single-photon counting (TCSPC) system. The fluorescence bursts exhibited a much longer lifetime than the background signal from DN-BODIPY in solution, thus suggesting that such a sudden intensity increase corresponds to the generation of fluorescent HN-BODIPY.

The precise mapping of photocatalytic activity in individual TiO_2 crystals at the nanometer scale were demonstrated by single-molecule fluorescence imaging (Figs. 2.3 and 2.4) [11, 12]. Interestingly, most fluorescence spots were found to be preferentially located on the (101) surface of the crystal (see red dots in image B). A similar tendency was observed for more than five individual examined crystals.

Metal–Semiconductor Metal−semiconductor heterostructures are promising visible light active photocatalysts for many chemical reactions. The photocatalytic behavior of metal−semiconductor heterostructures has been studied mainly at the ensemble level. The catalytic properties were considerably influenced by the individual particle sizes, structures, and so forth. To surmount the challenge arising from the intrinsic heterogeneity associated with ensemble-averaged measurements, it is highly desirable and necessary to employ photocatalytic measurements at the single-particle level.

The nature and photocatalytic properties of the surface reactive sites on single Au−CdS hybrid nano-catalysts were studied by high-resolution superlocalization fluorescence imaging (Fig. 2.5) [13]. The plasmon-induced hot electrons in Au are injected into the conduction band of the CdS semiconductor nanorod. The

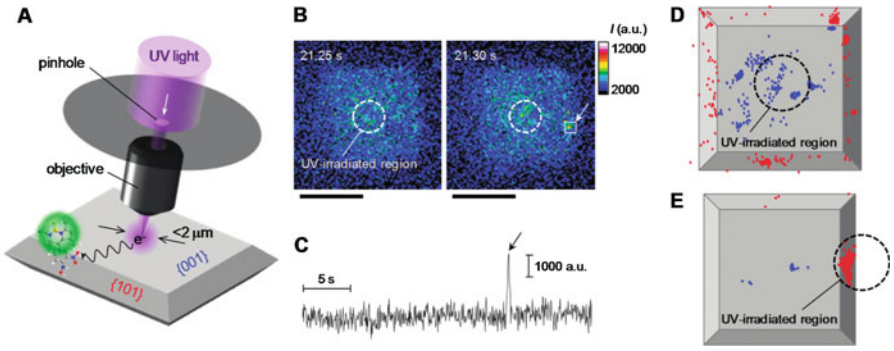

Fig. 2.4 (**a**) Illustration of the remote photocatalytic reaction on the {101} facets with DN-BODIPY during photoirradiation onto the {001} facets. The irradiated area was limited by a pinhole (the spot diameter is 2 μm on the crystal surface). (**b**) Fluorescence image of a TiO_2 crystal that is immobilized on the cover glass in Ar-saturated DN-BODIPY solution (1.0 μM, in methanol) under a 488 nm laser and UV irradiation. The scale bars are 4 μm. (**c**) Time trace of fluorescence intensity observed over the square region in panel B (see the arrow). The UV irradiation area is inside the white circle in the images. (**d** and **e**) Location of fluorescence bursts on the {001} (blue) and {101} (red) facets. The UV irradiation areas are inside the black circles (diameter 2 μm). (Reprinted with the permission from Ref. [12]. Copyright 2011 American Chemical Society)

specifically designed Au-tipped CdS heterostructures with a unique geometry (two Au nanoparticles at both ends of each CdS nanorod) provide more convincing high-resolution single-turnover mapping results and clearly prove the two charge-separation mechanisms. Engineering the direction of energy flow at the nanoscale can provide an efficient way to overcome important challenges in photocatalysis, such as controlling catalytic activity and selectivity. These results bear enormous potential impact on the development of better visible light photocatalysts for solar-to-chemical energy conversion.

Au-tipped CdS heterostructures were designed to clearly demonstrate the existence of two distinct photocatalysis mechanisms having the opposite direction of energy flow at the single-particle level, where two Au nanoparticles locate at both ends of each CdS nanorod. The relatively long distance between the two Au nanoparticles (186 nm on average) surmounts the obstacle caused by the single-molecule superlocalization accuracy (5–15 nm). Under the 532 nm laser irradiation, the h^+ reactive sites (circled blue cross) are positioned at the gold tips on both ends of the heterostructures, while the e^- reactive sites (circled red minus) are located along the inside length of the CdS nanorods within a distance of a few tens of nanometers from the Au tips. This result reveals the transfer of electron from Au to CdS. Opposite charge flowing direction was further verified when 405 nm laser was used since h^+ are distributed along the CdS nanorod, while the e^- reactive sites are located at both ends.

Imaging of Defect-Related Photocatalytic Activity Microporous titanosilicate ETS-10 is promising photocatalyst because of the inherent quantum nature of one-dimensional titania (–Ti–O–Ti–) wires in the framework and its high reaction

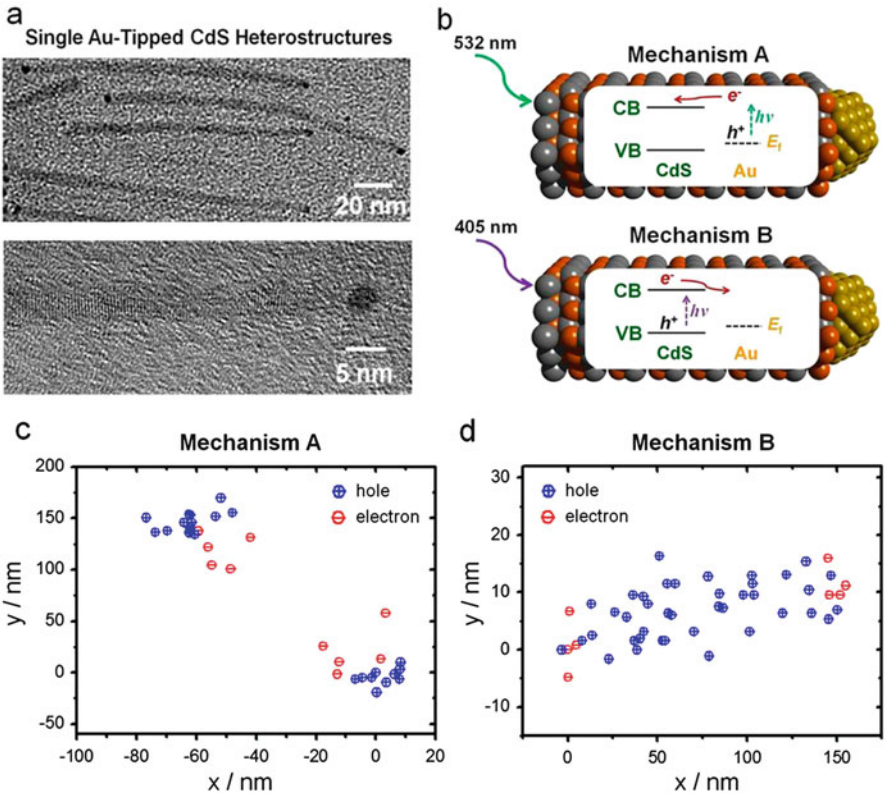

Fig. 2.5 (**a**) TEM image of typical single Au-tipped CdS nanorod. (**b**) Schematic illustrating two distinct photocatalysis mechanisms with the opposite direction of energy flow. In mechanism A at 532 nm, the photogenerated energetic electrons in Au are injected to the CB of the semiconductor. In mechanism B at 405 nm, the photogenerated electrons in the CB of the semiconductor are rapidly trapped by Au. (**c**) Super-resolution mapping of single reactive sites formed through mechanism A. (**d**) Super-resolution mapping of single reactive sites formed through mechanism B. (Reprinted with the permission from Ref. [13]. Copyright 2011 American Chemical Society)

selectivity owing to its nanoporous structure. The carriers formed from light irradiation migrate in the crystal through the wires. However, the wires may be randomly broken in the crystal because of inherent defects, which form active centers for molecular adsorption and redox reactions. To date, the influences of structural defects in ETS-10 on the adsorption and reaction dynamics of organic compounds have not been well characterized. The spatial heterogeneities of the surfaces and the inhomogeneous coupling interface between the adsorbed molecules and the nanoscale rough surfaces of the semiconductor make the dissecting of the complex interfacial ET processes highly difficult. The in situ fluorescence imaging of photocatalytic oxidation was carried out on single ETS-10 crystals using a redox-responsive fluorescent dye; 3′-(*p*-aminophenyl) fluorescein (APF), which was commonly used for the selective detection of $^{\bullet}$OH, was employed to identify the surface-

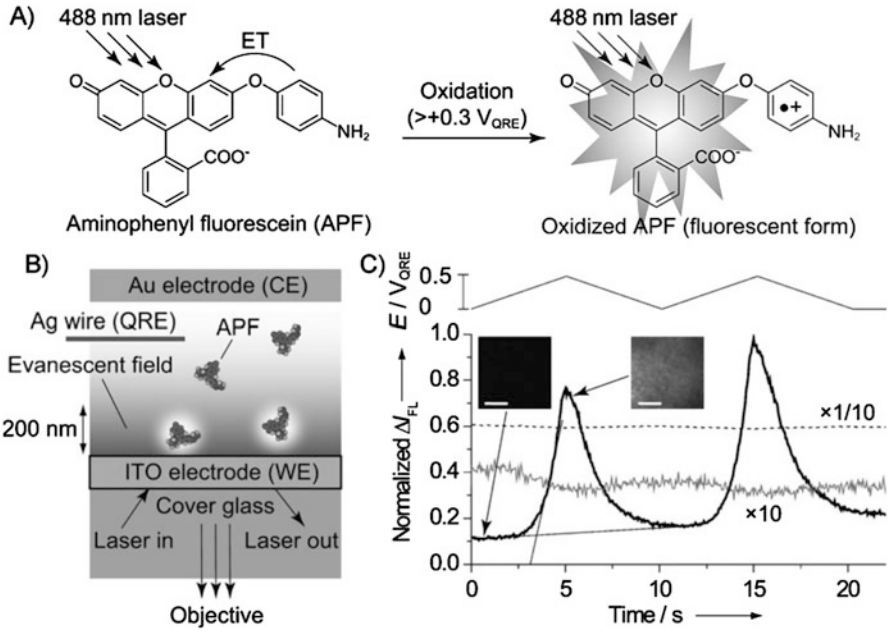

Fig. 2.6 (**a**) Reaction scheme for the one-electron oxidation of the p-aminophenyl moiety, which induces fluorescence in APF. ET = electron transfer. (**b**) Cell configuration for in situ spectroelectrochemical measurements under TIRFM. CE = counter electrode, QRE = quasi-reference electrode, WE = working electrode. (**c**) Applied potential dependence of normalized fluorescence intensity (IFL) obtained for the phosphate buffer solutions in the absence (gray line) and presence of APF (5 mm; solid line) or fluorescein (500 nm; dashed line). The images in (**c**) were acquired at a bin time of 50 ms. Scale bars are 5 mm. (Reproduced from Ref. [14] by permission of John Wiley & Sons Ltd)

active sites distributed over the ETS-10 (Fig. 2.6) [14]. It was revealed that surface treatment of ETS-10 with HF aqueous solution significantly increased not only the adsorption and reaction efficiencies but also the heterogeneity of photocatalytic activity among the crystals. The crystal defects serve as active sites during the photocatalytic reaction in aqueous solution. The fluorescence intensity of fluorescein increased gradually upon UV irradiation of phosphate buffer solutions containing APF and ETS-10 powder. In the absence of ETS-10, the fluorescence intensity did not increase at all, thus suggesting that fluorescein molecules might be generated by the reaction of photoexcited ETS-10 and APF molecules. Meanwhile, a significant increase in the fluorescence intensity was observed for HF-treated ETS-10 because of the exposure of surface-active sites such as titanols and larger micropores by partial dissolution of siliceous walls surrounding the titania wires (Fig. 2.7).

The Diffusion Distance of Radicals in a Single Particle Porous, cavitary, and tubular structured photocatalysts with a high specific surface area have been designed to improve the photocatalytic efficiency or achieve the selective transformation. These kinds of materials are supposed to have more active sites for the

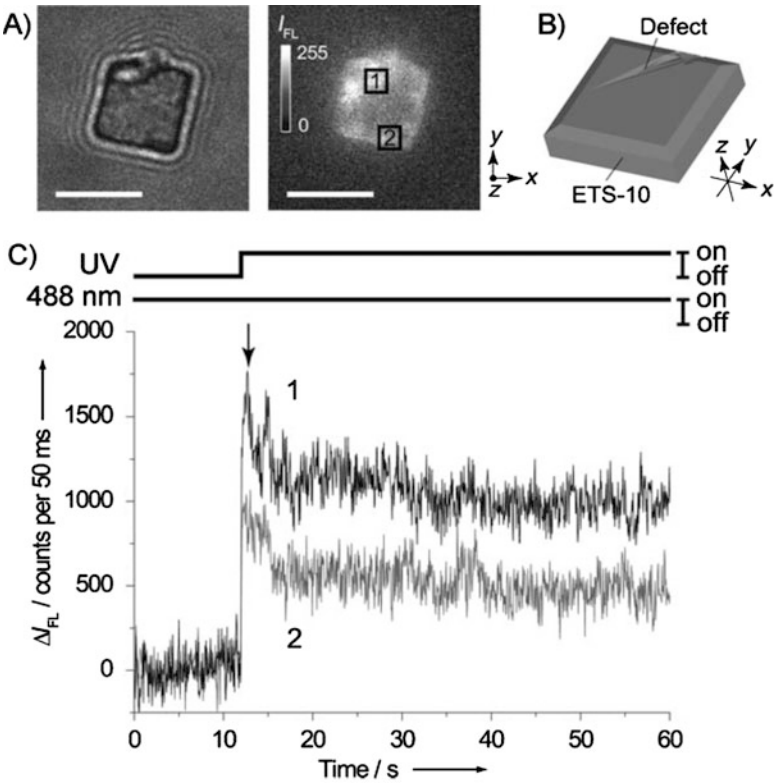

Fig. 2.7 (**a**) Transmission image (left) and fluorescence image under UV irradiation (right), where the imaging focal plane was located at the center of the crystal. The arrow in (**c**) denotes the time when the fluorescence image was acquired. Scale bars correspond to 5 mm. (**b**) Spatial configuration of the crystal (see the axes). (**c**) Time traces of the fluorescence intensity acquired at the defect (position 1, black line) and near the edge of the ETS-10 crystal (position 2, gray line). (Reproduced from Ref. [14] by permission of John Wiley & Sons Ltd)

adsorption and activation of reactants. However, the performance is highly dependent on the accessibility of reactant molecules to the active sites inside the bulk particles. The structural disorders or defects homogeneously distributed over the framework often hinder the efficient molecular transport. One of the examples for the single-molecule imaging of photocatalytic reactions in a porous TiO_2 nanotube was achieved using fluorescein and TIRFM [15]. Single TiO_2 nanotube was placed in a custom-made sample chamber, which is irradiated by UV light with a wavelength of 365 nm and laser light with a wavelength of 488 nm to excite the nanotube and fluorescein, respectively (Fig. 2.8). It is expected that the photocatalytic reaction will occur randomly on the entire nanotube. To examine the specific interaction between the wall of the TiO_2 nanotube and the fluorescein diffusing in the macropore, SiO_2 nanotube without mesopores was used as a control. Fluorescein was generated by auto-oxidation after intense UV irradiation. Both TiO_2 and SiO_2 nanotubes exhibit a

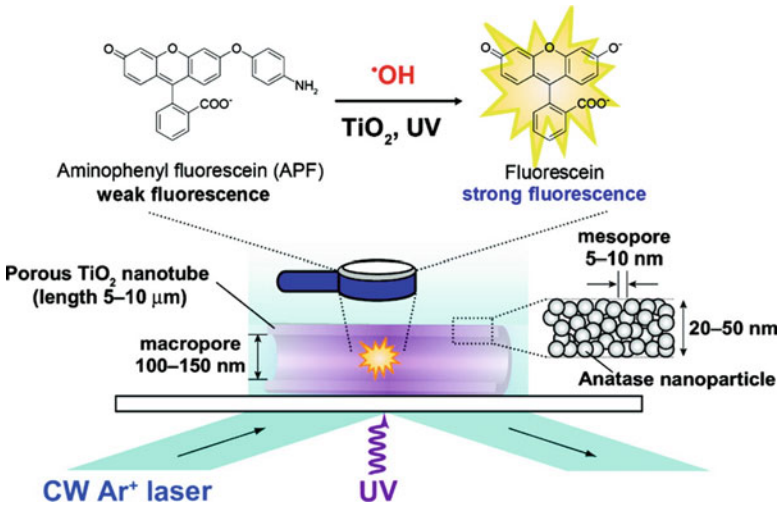

Fig. 2.8 Schematic representation of photocatalytic reaction occurring on a single nanotube. (Top) generation of emissive fluorescein induced by the photocatalytic reaction in the porous structure of the TiO_2 nanotube. (Bottom) the porous TiO_2 nanotube on the cover glass is simultaneously irradiated with UV light (wavelength: 365 nm) and evanescent light produced by a CW Ar^+ laser (wavelength: 488 nm) to excite the nanotube and fluorescein, respectively. (Reprinted with the permission from Ref. [15]. Copyright 2011 American Chemical Society)

similar distribution, confirming that the fluorescein in the macropore of the TiO_2 nanotube diffuses without interaction with the surface.

2.2 Infrared Spectroscopy

Infrared (IR) spectroscopy is a powerful method to study adsorbed species on solid surfaces, which has the ability to provide the vibrational spectrum of both reactants and photocatalyst. Abundant information can be real-time revealed regarding the molecular structure, orientation, and conformation of surface species through the in situ IR spectroscopy. Techniques including electron paramagnetic resonance (EPR), X-ray absorption near K-edge structure spectroscopy, absorption, and emission spectra only allow hypotheses to be formulated regarding the identity of surface intermediate species, but their chemical nature could not be directly specified. By contrast, the electric fields generated by photoexcited charge carriers and the further reaction of charge carrier with surface hydroxyl and adsorbed molecules may cause the intensity and wavelength shifts of stretching vibrations and the formation of new band in IR spectroscopy, thus allowing the inferring of the possible reaction path based on the intermediates found from the in situ FTIR study.

2.2.1 Gas-Phase Photocatalysis

Using the diffuse reflectance IR Fourier transform spectroscopy (DRIFTS), the gas-phase photocatalytic reaction can be well tracked. Szczepankiewicz et al. revealed a new band at 3716 cm^{-1} for UV-irradiated TiO_2 in the gas phase in the presence of a hole scavenger, ascribing to OH stretching for surface $Ti^{3+}-OH$ formed by electron capture at acidic $Ti^{4+}-OH$ centers [16]. Another band at 3683 cm^{-1} in an oxygen atmosphere in the absence of hole scavengers was attributed to a surface-bound OH radical formed by hole capture at $Ti^{4+}-OH$ centers. Intensity changes and corresponding wavelength shifts for $\nu(TiO-H)$ are proportional to the magnitude and polarity of the electric field. Wu et al. detected a large amount of surface peroxo species and OH groups on the TiO_2 and M (Cu, V, and Cr)/TiO_2 catalysts after a calcination treatment at 500 °C under airflow. The photocatalytic reaction of nitric oxide (NO) on TiO_2 and transition metal-loaded M/TiO_2 catalysts indicates nitric oxide is adsorbed on TiO_2 and M/TiO_2 in the form of bidentate nitrites and nitrates by reacting with OH groups, peroxo, or M = O species. In addition, NO can also be adsorbed on M^{n+} in the form of nitrosyls. Under UV irradiation, bidentate nitrite was oxidized to either monodentate or bidentate nitrate, which was induced by superoxo species oxidized from peroxo species by photogenerated holes.

2.2.2 Aqueous-Phase Photocatalysis

The application of IR spectroscopy in aqueous or vapor photocatalysis system is restricted by the strong IR absorption for water. To minimize the interference from water, the attenuated internal reflection (ATR) technique has been developed for dissecting the intermediate formed during photoirradiation, where evanescent IR waves penetrate intro a thin layer of an aqueous solution and reach the surface of semiconductor covered on the surface of the internal reflection element (IRE). The spectral cell for multiple internal reflection infrared (MIRIR) experiments uses a trapezoidal-shaped ZnSe as the internal reflection element (IRE), which was irradiated by an IR beam with 45° incident angle. Taking TiO_2 film as a demonstration, it is applied on one face of the IRE by a dip-coating method (Fig. 2.9), which was set in the spectral cell made by Diflon [17]. The inner volume of the cell was approximately 10 mL. The length and width of the exposed area of the IRE are 35.5 and 9.2 mm, respectively. The IR light was reflected about nine times in the IRE with TiO_2, as calculated from the geometry of the IRE. The spectral cell was placed in the sample chamber of an FTIR spectrometer with a deuterated triglycine sulfate (DTGS) detector.

The first direct in situ spectroscopic detection of primary intermediates for the photocatalytic O_2 reduction in aqueous solutions was achieved in TiO_2 system through IRE technology. Under the UV irradiation and in the presence of dissolved

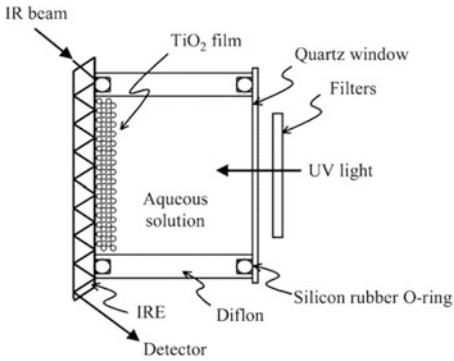

Fig. 2.9 Schematic illustration of a spectral cell used for in situ MIRIR measurements [17]. (Reprinted with the permission from Ref. [17]. Copyright 2011 American Chemical Society)

O_2, new peaks at 943, 838 and 1250–1120 cm^{-1} appeared together with intensity changes in other bands. Investigations of influences of the solution pH, the presence or absence of hole and electron scavengers, and isotopic exchange between H_2O and D_2O on the spectral changes have revealed that the primary step of photocatalytic O_2 reduction is the formation of the surface peroxo species, giving the 943 cm^{-1} band, probably with the surface superoxo species as a precursor, in neutral and acidic solutions. The surface peroxo species is then transformed to the surface hydroperoxo, TiOOH, giving the 838 and 1250–1120 cm^{-1} bands, by protonation in the dark.

To enhance the detection sensitivity, surface-enhanced IR absorption (SEIRA) has been utilized for molecules adsorbed on a thin noble metal (Au, Ag) film with abundant free electron. When SEIRA spectroscopy (SEIRAS) is carried out in ATR configurations, it has a great advantage that IR measurements can be carried out even in an aqueous solution, because an IR beam hardly passes through the solution. For example, SEIRAS was applied to in situ observation of surface species formed during the photocatalytic decomposition of acetic acid over bare TiO_2 [18], Au/TiO_2, and $Au/Pt/TiO_2$ films, on which an Au island film was deposited. For a gas-phase reaction, an evacuable IR cell was used, which was connected to a pumping and gas handling system. SEIRAS measurements were carried out in a backside reflection mode, in which an IR beam from FTIR was introduced from the CaF_2 side of the sample at the incident angle of ca. 50° and reflected at the interface between the TiO_2 and Au films. The reflected IR beam was collimated to an external MCT detector at liquid nitrogen temperature. SEIRA spectra were recorded with the resolution of 4 cm^{-1}. The adsorption states of acetic acid were determined in both the liquid and gas phase, and molecular adsorption was found to be dominant in the gas phase. Pt deposition on the TiO_2 film led to the formation of adsorbed methyl during the photodecomposition of gas-phase acetic acid, indicative of the formation of methyl radical as a reaction intermediate. The addition of gas-phase water to the system led to a significant increase in the coverage of adsorbed methyl as a result of enhancement in the reaction rate as reported before. Since the metal films used in SEIRAS are discontinuous and island-structure, SEIRAS can detect chemical species, which exist not only on the metal films but also in the vicinity of the metal

islands. Water and acetic acid were deaerated by repeating a freeze-and-thaw cycle for a gas-phase reaction. The vapor of water or acetic acid was introduced into the cell from a gas handling system equipped with a Baratron pressure gauge. A 1:1 mixture of gas-phase water and acetic acid was prepared by mixing their vapor at the same pressure in a glass reservoir. The light source was a high-pressure Hg lamp (Ushio UIV-570) that was filtered through a band-pass filter (Toshiba UV-D33S, 240–400 nm) and a water filter (10 cm long) to remove heat.

Primary intermediates of oxygen photoevolution (water photooxidation) reaction in the interface of TiO_2 (rutile) and aqueous solution were investigated by in situ multiple internal reflection infrared (MIRIR) absorption and photoluminescence (PL) measurements [19]. UV irradiation of TiO_2 in the presence of 10 mM Fe^{3+} in the solution caused the appearance of a new peak at 838 cm^{-1} and a shoulder at 812 cm^{-1}. Detailed investigations of the effects of solution pH, the presence of methanol as a hole scavenger, and isotope exchange in water between $H_2{}^{16}O$ and $H_2{}^{18}O$ on the spectra have shown that the 838 and 812 cm^{-1} bands can be assigned to the O–O stretching mode of surface TiOOH and TiOOTi, respectively, produced as primary intermediates of the oxygen photoevolution reaction. The results give strong support to our previously proposed mechanism that the oxygen photoevolution is initiated by a nucleophilic attack of a H_2O molecule on a photogenerated hole at a surface lattice O site, not by oxidation of surface OH group by the hole. The conclusion is supported by PL measurements. A plausible reaction scheme is proposed for the oxygen photoevolution on TiO_2 (rutile) in aqueous solutions of pH less than about 12.

Semiconductor electrodes capable of using solar photons to drive water-splitting reactions have been the subject of tremendous interest over recent decades. The surface has been found to play a significant role in determining the efficiency of water oxidation. However, previous works have only allowed hypotheses to be formulated regarding the identity of relevant surface species. The first observation of a surface intermediate of oxygen evolution at an Ir oxide multi-electron catalyst was reported by Sivasankar et al. [20], where a surface hydroperoxide intermediate has been detected upon oxidation of water at an Ir oxide nanocluster catalyst system under pulsed excitation of a $[Ru(bpy)_3]^{2+}$ visible light sensitizer by recording of the O–O vibrational mode at 830 cm^{-1}. Rapid-scan FTIR spectroscopy of colloidal H_2O, D_2O, and $D_2{}^{18}O$ solutions in the attenuated total reflection mode allowed spectral assignment of IrOOH on the basis of an observed D shift of 30 cm^{-1} and ^{18}O shifts of 24 cm^{-1} ($^{16}O^{18}O$) and 46 cm^{-1} ($^{18}O^{18}O$) (Fig. 2.10). The laser pulse response of the infrared band is consistent with the kinetic relevancy of the intermediate.

For Co_3O_4, two surface intermediates of visible light-sensitized water oxidation were detected by rapid-scan FTIR spectroscopy. The agreement of the ^{18}O isotopic composition of a surface superoxide species and the final O_2 gas product provides evidence for the kinetic competency of the three-electron oxidation intermediate. At a fast catalytic site absorbing at 1013 cm^{-1}, the superoxide intermediate grows and O_2 evolves within a 300 ms photolysis pulse. By contrast, a slow site marked by a Co (IV) = O group does not advance beyond the one-electron intermediate absorbing at

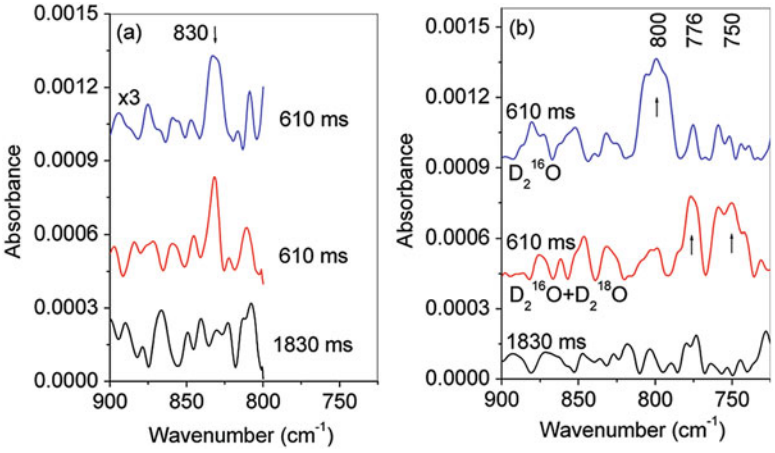

Fig. 2.10 Rapid-scan FTIR traces in the 900–700 cm^{-1} region. (**a**) 610 ms (light on) and 1830 ms spectra (light off) for the photooxidation of H_2O. The 610 ms slices from two separate experiments are shown to indicate the degree of uncertainty regarding band shape. The spectral region below 800 cm^{-1} exhibits high noise due to H_2O tumbling-mode absorption. (**b**) 610 ms slices of experiments in $D_2{}^{16}O$ (top, average of 140 runs) and $D_2{}^{16}O$ (33%) + $D_2{}^{18}O$ (66%) (middle, average of 68 runs), along with the 1830 ms slice of the $D_2{}^{16}O$ experiment (bottom). (Reprinted with the permission from ref. [20]. Copyright 2011 American Chemical Society)

840 cm^{-1} within the same 300 ms pulse. The widely different photocatalytic efficiency of the two types of sites is attributed to the presence/absence of adjacent Co(III)OH groups coupled via an oxygen bridge. Improvement of the sensitivity of the ATR method should allow time-resolved FTIR monitoring with shorter photolysis pulses, which, in turn, will enable detection and kinetic analysis of the early (one- and two-electron) surface intermediates of the fast site [21].

Despite of the successful determination of surface intermediates by IR technique, the role of the surface intermediate species in the photocatalytic water-oxidation reaction was rarely established definitively. α-Fe_2O_3 with excellent stability and elemental abundance has emerged as one of the most promising materials to carry out the light-driven water-oxidation half reaction for photoelectrochemical (PEC) water splitting. The combination of suitable optical and electrochemical properties enables the possibility of sustainable hydrogen production in a hematite-based PEC cell. However, so far the efficiencies measured with hematite have fallen well short of the theoretical maximum. For example, state-of-the-art systems produce only 30% of the maximum photocurrent that can be generated under water splitting with hematite. The cause of this poor performance has been the focus of extensive studies during the past decade. Bulk recombination and surface recombination have both been found to limit the quantum efficiency of photogenerated charge-carrier separation and the output power. Bulk recombination results in a near-zero minority carrier (hole) diffusion length, which limits the charge-collection length to the space-charge layer in the hematite–electrolyte interface. Surface recombination is in competition with the forward water-oxidation hole-transfer reactions and accounts

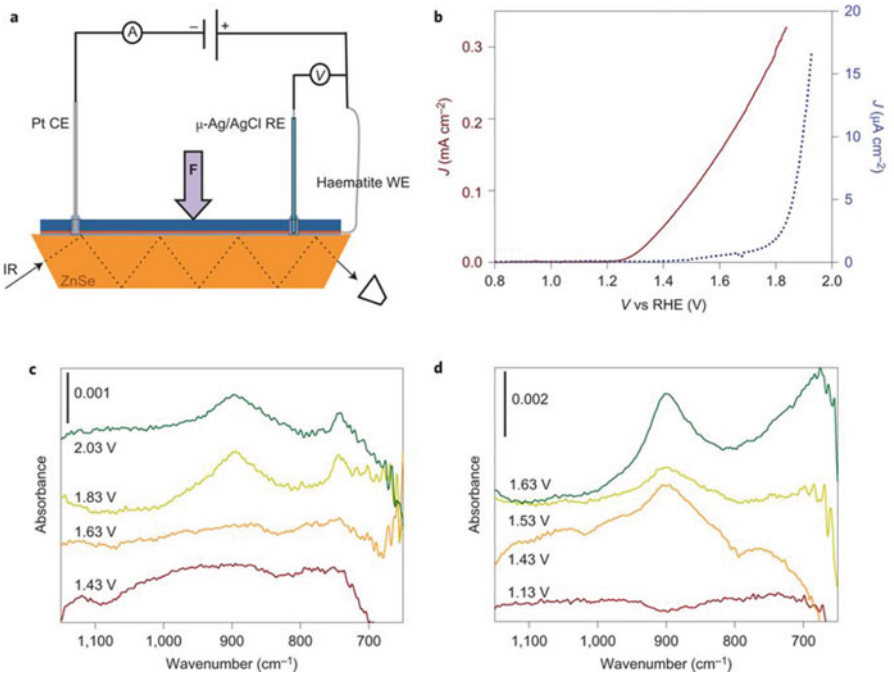

Fig. 2.11 (**a**) Experimental setup and results of infrared spectroscopy measurements during electrochemical and PEC water oxidation, where ZnSe is the ATR crystal. (**b**) J–V curves of a hematite electrode in the operando PEC infrared setup measured in contact with D_2O in the dark (blue) and under illumination (dark red). (**c**) Infrared spectra of hematite scanned at constant applied potentials, from 1.43 to 2.03 V versus RHE, in the dark. (**d**) Under illumination. (Reprinted from Ref. [22], with kind permission from Springer Science+Business Media)

for the loss of several hundred millivolts of photovoltage. A clear understanding of the surface chemistry of hematite during PEC water oxidation is thus crucial as it determines the extent of band bending and of Fermi-level pinning, which control the charge-separation and hole-collection (water-oxidation) efficiencies. The potential- and light-dependent water-oxidation reaction under photoelectrochemical (PEC) was monitored on α-Fe_2O_3 through MIRIR technology (Fig. 2.11). A prominent peak in the spectra was resolved reproducibly at 898 cm^{-1}, which grew in at applied potentials positive to the onset of the water-oxidation current (1.7 V and 1.25 V versus RHE in the dark and under illumination, respectively). The potential- and light-dependent peak evolution is consistent with electrochemically or photoelectrochemically generated species on the electrode surface. That the absorption peaks are only observed positive of the onset potential of the water-oxidation current indicates that this absorption peak is associated with species involved in the D_2O oxidation reaction. An additional peak at 743 cm^{-1} was observed with variable signal-to-noise ratios for the different experiments performed, which we attribute to

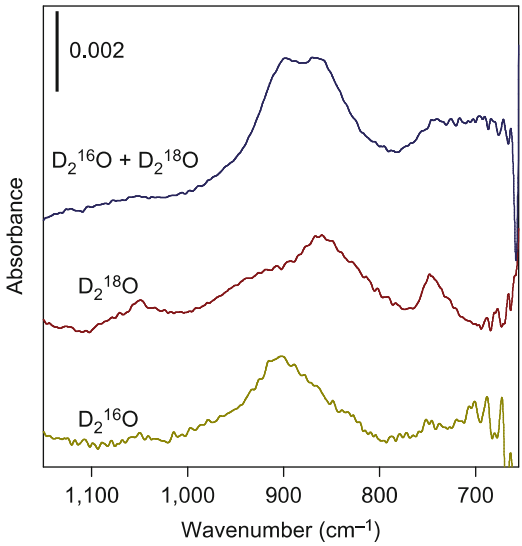

Fig. 2.12 Plot of the effect of oxygen isotopic variation on the infrared absorption spectra during PEC water oxidation with hematite electrodes. The spectra were measured at an applied potential of 1.63 V versus RHE under illumination in contact with $D_2{}^{16}O$, $D_2{}^{18}O$, or a 1:1 ratio of $D_2{}^{16}O/D_2{}^{18}O$. (Reprinted from Ref. [22], with kind permission from Springer Science +Business Media)

its proximity to the spectral cutoff region and is thus strongly affected by any traces of H_2O incorporated in the cell.

In the absence of temporal resolution, the kinetic relevancy or position of these species in the photocatalytic cycle could not be addressed. Yet, knowledge of individual events in the four-electron cycle of water oxidation on the catalyst surface through observation of structurally identified species and their temporal behavior is required to uncover kinetic bottlenecks and to provide insights regarding design changes to overcome them. Isotope-labeling experiments using ^{18}O-labeled and ^{16}O-labeled water were used for the peak assignments to distinguish Fe = O and Fe–O–OH groups with overlapped vibration frequency in the range of 750–900 cm^{-1} and 740–950 cm^{-1}, respectively (Fig. 2.12). The $^{16}O/^{18}O$ shift for Fe = O is expected to be ~40 cm^{-1}. The frequency shift associated with O–O isotope exchange is between 20 and 30 cm^{-1} for partially labeled (^{16}O–^{18}O) and between 44 and 61 cm^{-1} for fully labeled (^{18}O–^{18}O) groups. Operando spectra collected in contact with $D_2{}^{18}O$ exhibited absorption peaks at 743 and 857 cm^{-1}. The peak at 857 cm^{-1} in $D_2{}^{18}O$ is shifted by 42 cm^{-1} compared with the spectrum taken in $D_2{}^{16}O$. This shift is consistent with either Fe = ^{16}O to Fe = ^{18}O or Fe–^{16}O–^{16}O to Fe–^{18}O–^{18}O, both of which are possible intermediate species of water oxidation on hematite. Further study performed in a 1:1 ratio of $D_2{}^{16}O/D_2{}^{18}O$ produced an equally weighted doublet with peaks at 898 and 857 cm^{-1}, which are thus assigned as Fe = ^{16}O and Fe = ^{18}O, respectively, since the peroxide is supposed to produce three different vibrations that correspond to ^{16}O–^{16}O, ^{16}O–^{18}O, and ^{18}O–^{18}O stretching modes with a 1:2:1 ratio of intensities [22].

2.3 Raman

Raman spectroscopy utilizing the inelastic scattering of light was first developed in 1912 by the Indian physicist C. V. Raman [23]. Although Raman can provide the fingerprint spectrum interference-free from water, the tiny Raman cross-section area limits its broad application in chemical analysis for a long period since its invention. The integration of Fourier transform technology, charge-coupled device (CCD) detectors, compact spectrographs, effective laser rejection filters, near-infrared lasers, and small computers greatly push forward to the applicability of Raman spectroscopy in chemical analysis [24]. The enhancement of the inelastic scattering probability can be further achieved from resonance Raman (RR) scattering, where the incident laser is near an electronic transition of the molecule of interest, increasing the signal by an additional factor of 10^2–10^6. The surface-enhanced Raman spectroscopy (SERS) and tip-enhanced Raman spectroscopy (TERS) allow the possibility of the single-molecule detection [25], which use plasmonically enhanced Raman scattering to characterize the chemical information on single molecules.

Regarding the reaction tracking, the priority of Raman technology based on the molecular vibration and rotation lies in the fingerprint spectra interference-free from water. However, Raman spectroscopy usually gives rise to strong signals of inorganic catalyst instead of surface chemical probes, preventing it from the application in tracing the transformation path of the surficial species.

Currently, SERS has mainly used for in situ monitoring the kinetics of noble metal (Au, Ag)-catalyzed photocatalytic reaction on the basis of the surface plasmon resonance (SPR) effect [26]. In this way, SPR has the dual function of activating the chemical reaction and enhancing the Raman signal of surface species. O_2 have been found to be involved into the SPR-catalyzed oxidation reaction, but the activation mechanism/path of oxygen molecules is still obscure due to the extremely short lifetime of SPR-induced hole–electron pair. Using SPR-assisted selective oxidation of *p*-aminothiophenol (PATP) as a demonstration, SERS was used for the in situ tracking of the O_2 evolution (Fig. 2.13). Both experiments and DFT calculations reveal that O_2 were activated by accepting an electron from a metal nanoparticle under the excitation of SPR to form a strongly adsorbed oxygen molecule anion. The anion was then transformed to Au or Ag oxides or hydroxides on the surface to oxidize the surface species, which was also supported by the heating effect of the SPR (Fig. 2.14).

Using the PATP oxidation SPR-catalyzed by Ag nanoparticle as a model reaction, a radical-capturer-assisted SERS has been used as an in situ tracking technique to explore the primary active species determining the reaction path [27]. Hole is revealed to be directly responsible for the oxidation of PATP to DMAB and O_2 functions as an electron capturer to form isolated hole. The oxidation degree of PATP can be further enhanced through a joint utilization of electron capturers of $AgNO_3$ and atmospheric O_2, producing *p*-nitrothiophenol (PNTP) within 10 s due to the improved hole–electron separation efficiency (Fig. 2.15).

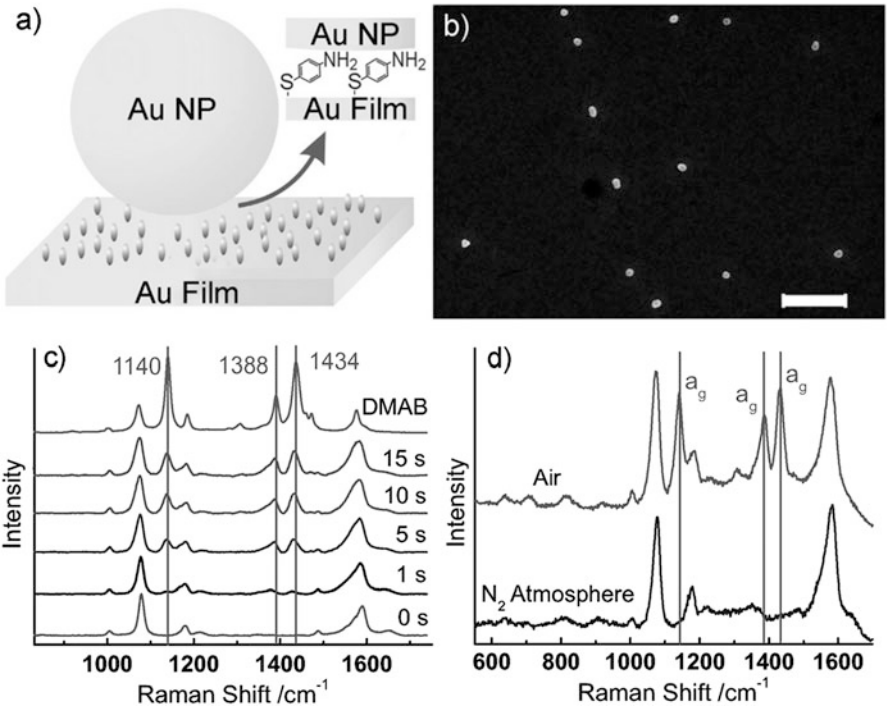

Fig. 2.13 (**a**) Au/PATP/Au nanoparticle, (**b**) SEM image (the scale bar is 500 nm), and (**c**) illumination-time-dependent Raman spectra and (**d**) comparative Raman spectra of Au/PATP/Au NPs recorded in air and N_2 atmosphere. (Reproduced from Ref. [26] by permission of John Wiley & Sons Ltd)

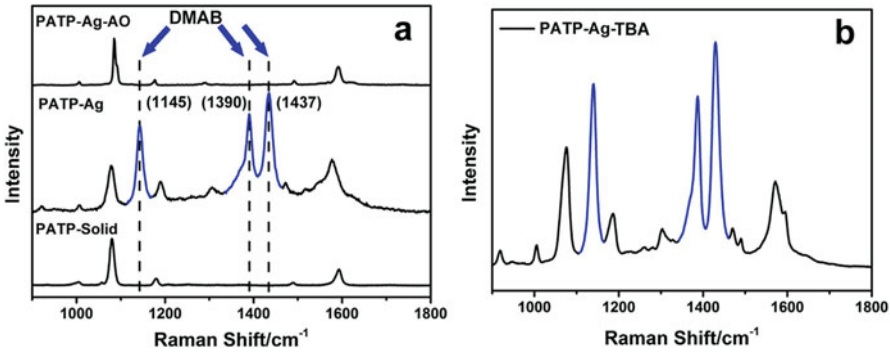

Fig. 2.14 (**a**) Raman signal of PATP solid (black line), SERS signals of PATP on Ag nanoparticle layer in the absence and presence of AO; (**b**) SERS signal of PATP on assembly Ag nanoparticle layer in the presence of TBA. (Reprinted from Ref. [27], with kind permission from Springer Science+Business Media)

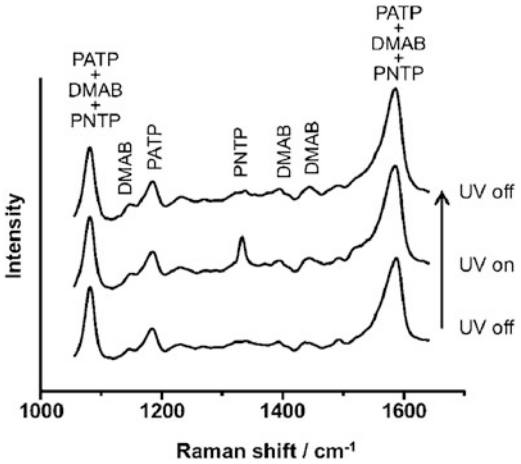

Fig. 2.15 SERS spectra recorded for TiO_2-Au NPs that had been functionalized with PATP: before UV illumination (bottom trace), under UV illumination (middle trace), and after the UV illumination was turned off (top trace). Before UV excitation, only peaks assigned to PATP were detected (DMAB peaks displayed very low intensities). Under UV exposure for 5 min, the formation of PNTP was detected. PNTP could be further reduced to DMAB as the UV illumination was removed (red trace). All spectra employed 1 mW and 1 $mWcm^{-2}$ as the laser and UV illumination power, respectively. (Reproduced from Ref. [28] by permission of John Wiley & Sons Ltd)

Although catalytic processes mediated by SPR excitation have emerged as a new frontier in catalysis, the selectivity of these processes remains poorly understood. The selectivity of the SPR-mediated oxidation of PATP employing Au NPs as catalysts was controlled by the choice of catalysts (Au or TiO_2-Au NPs) and by the modulation of the charge transfer from UV-excited TiO_2 to Au [28]. When Au NPs were employed as catalyst, the SPR-mediated oxidation of PATP yielded DMAB. When TiO_2-Au NPs were employed as catalysts under both UV illumination and SPR excitation, PNTP was formed from PATP in a single step. Interestingly, PNTP molecules were further reduced to DMAB after the UV illumination was removed. Therefore, the control over charge-transfer processes may play an important role to tune activity, product formation, and selectivity in SPR-mediated catalytic processes.

Semiconductors including TiO_2, Cu_2O, and MoO_{3-x} have also proven to be SERS active [29–32]. It is desirable to in situ and real-time (operando) reveal the interfacial information between semiconductor and surficial reactants through SERS, which is extremely significant for guiding the photocatalyst design. However, restricted by the low sensitivity, there is no study about SERS self-tracking of the photocatalytic process on semiconductor. A novel Ag-alumina hybrid SERS platform has been designed for the spectroscopic detection of surface reactions in the steady state [33]. Single crystalline and faceted silver (Ag) nanoparticles with strong light scattering were prepared in large quantity, which enables their reproducible self-assembly into large-scale monolayers of Raman sensor arrays by the Langmuir–

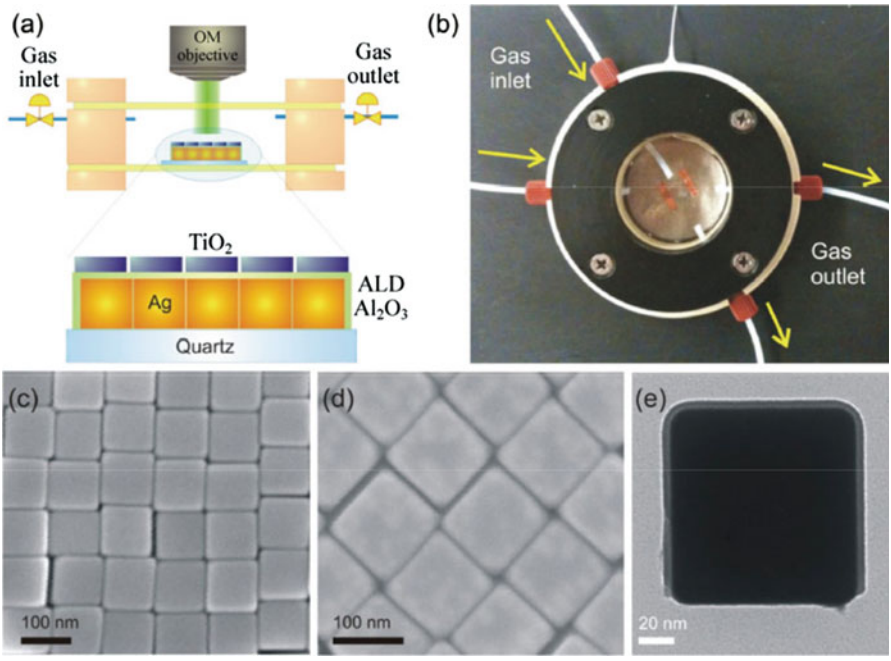

Fig. 2.16 (**a**) Scheme and (**b**) photograph of the experimental cell, where the Ag nanocube Langmuir–Blodgett film was first coated with a ~3 nm layer of Al_2O_3 by ALD deposition, follow by Langmuir–Blodgett assembly of square TiO_2 nanocrystals. The sample was placed on the bottom quartz slide, and deoxygenated solution was added. The chamber was closed and blown with Ar gas for at least 15 min prior to UV irradiation. SEM images of (**c**) the Ag nanocube film made by the Langmuir–Blodgett technique and (**d**) Ag nanocube film after Al_2O_3 coating. (**e**) TEM image of an Al_2O_3-coated Ag nanocube peeled off from the quartz slide. (Reprinted from Ref. [33], with kind permission from Springer Science+Business Media)

Blodgett technique. The closely packed sensor film contains high density of sub-nm gaps between sharp edges of Ag nanoparticles, which created large local electromagnetic fields that serve as "hot spots" for SERS enhancement. The SERS substrate was then coated with a thin layer of alumina by atomic layer deposition to prevent charge transfer between Ag and the reaction system (Fig. 2.16). The photocatalytic water-splitting reaction on a monolayer of anatase TiO_2 nanoplates decorated with Pt cocatalyst nanoparticles was employed as a model reaction system. Reaction intermediates of water photooxidation were observed at the TiO_2/solution interface under UV irradiation. The surface-enhanced Raman vibrations corresponding to peroxo, hydroperoxo, and hydroxo surface intermediate species were observed on the TiO_2 surface, suggesting that the photooxidation of water on these anatase TiO_2 nanosheets may be initiated by a nucleophilic attack mechanism.

Recently, TiO_2 with cavitary structure has been revealed to be highly SERS sensitive with an enhance factor over 10^4 due to the improved light scattering efficiency, which provides possibility for the operando self-monitoring of the

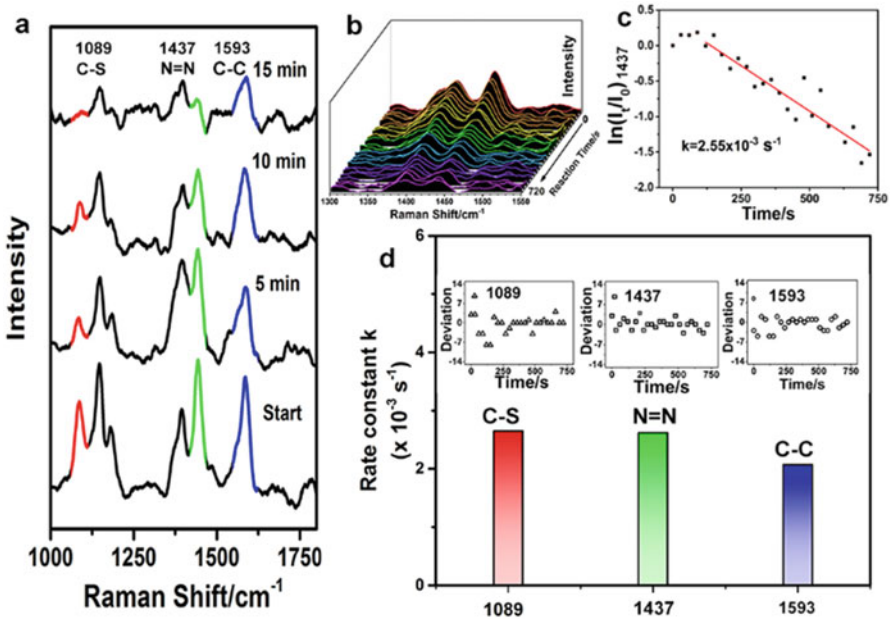

Fig. 2.17 (**a**) SERS spectra of PATP on TiO_2 IO under the irradiation of 532 nm laser for 15 min with a time interval of 5 min. (**b**) Evolution of $\nu_{N=N}$ peak recorded with a time interval of 30 s. (**c**) The logarithm of $(I_t/I_0)_{1437}$ processed using the normalized vibration peak intensity of TiO_2 at 146 cm^{-1} as an internal control. (**d**) Reaction rate constants for the cleavage of C–S, N=N, and C–C bonds under the long-time irradiation of 532 nm laser with a power of 5.0 mW and the corresponding wavenumber deviation collected at different time (inset). (Reprinted with the permission from Ref. [35]. Copyright 2011 American Chemical Society)

photocatalysis reaction [34]. The utilization of the fingerprint spectrum for the operando monitoring of a photocatalytic process is extremely desired to accurately understand the reaction mechanism but long remains challenging. Ordered macroporous TiO_2 that is concomitantly photocatalytically active and highly SERS sensitive was employed to self-track the photocatalytic reaction using the oxidation of PATP as the model [35]. The photocatalytic degradation under 532 nm laser irradiation initiated from the formation of the azo compound was explicitly revealed by finely resolved SERS spectra (Fig. 2.17). More importantly, the decomposition rates of different bonds including N=N, C–S, and C–C were, respectively, determined, following a first-order kinetics process with the rates in the range of 2.1 ~ 2.7 × 10^{-3} s^{-1}. Meanwhile, this self-monitoring strategy also provides an opportunity for gaining an insight into the effect of photothermal catalysis on selective formation of the azo compound.

Fundamental understanding of the energetic/electronic coupling properties of a molecule−semiconductor interface is of great importance. The changes in molecular conformations and vibrational modes can have significant impact on the interfacial charge-transfer reactions. Using single-hot-spot microscopic surface-enhanced

Raman spectroscopy (SMSERS), the change in the interface properties of alizarin−TiO_2 system can be probed as a result of the externally applied electric field [36]. The perturbation, caused by the external potential, has been observed as a shift and splitting of the 648 cm^{-1} peak, typical indicator of the strong coupling between alizarin and TiO_2. On the basis of the experimental results and DFT calculations, the presence of perturbed alizarin−TiO_2 coupling under interfacial electric potential may lead to changes in the interfacial electron transfer dynamics. Additionally, heterogeneously distributed dye molecules at the interface on nanometer length scale and different molecule–semiconductor binding interactions under charge accumulation associated interfacial electric field changes create intrinsically inhomogeneous interfacial ET dynamics associated with both static and dynamic disorders.

2.4 In Situ Atomic Force Microscopy and Fluorescence

Combining the single-molecule fluorescence spectroscopy approach with various other techniques such as computational studies, atomic force microscopy (AFM), electrochemistry, and Raman spectroscopy can facilitate inspection of multiple parameters with high chemical selectivity and wide temporal and spatial resolutions. Significant efforts made in this direction have already indicated the importance of various factors in determining injection dynamics and physical origins for interfacial ET rate fluctuations.

The fundamental information related to the energy flow between molecules and substrate surfaces as a function of surface site geometry and molecular structure is critical for understanding interfacial ET dynamics. The inhomogeneous nanoscale molecule−surface and molecule−molecule interactions are presumably the origins of the complexity in interfacial ET dynamics; thus, identifying the environment of molecules at nanoscale is crucial. It is challenging to correlate the observed heterogeneity of interfacial CT dynamics to the material and interfacial structures based on fluorescence measurement alone. The AFM correlated single-molecule fluorescence intensity/lifetime imaging microscopy (AFM-SMFLIM) is capable of identifying and characterizing individual molecules distributed across the heterogeneous surface at the nanometer length scale. Nanoscale morphology and interfacial ET dynamics at a single-molecule level can be observed. Moreover, the blinking behavior and lifetime of each molecule in combination with the topography of the environment at nanoscale provide the location of each molecule on the surface at nanoscale and the coupling strength of each molecule with TiO_2 nanoparticles.

Using single CdSe/CdS quantum dot (QD) functionalized atomic force microscopy (AFM) tips, the spatial dependence of photoinduced electron transfer dynamics from the single QD to TiO_2 nanoparticles can be controlled and probed with high spatial (sub diffraction-limited) and temporal (limited by fluorescence microscopy) resolutions (Fig. 2.18) [37]. CdSe/CdS QDs with a CdSe core (∼1.2 nm in radius) and six monolayers of CdS (2.2 nm in thickness) were attached on the n-Si AFM tip

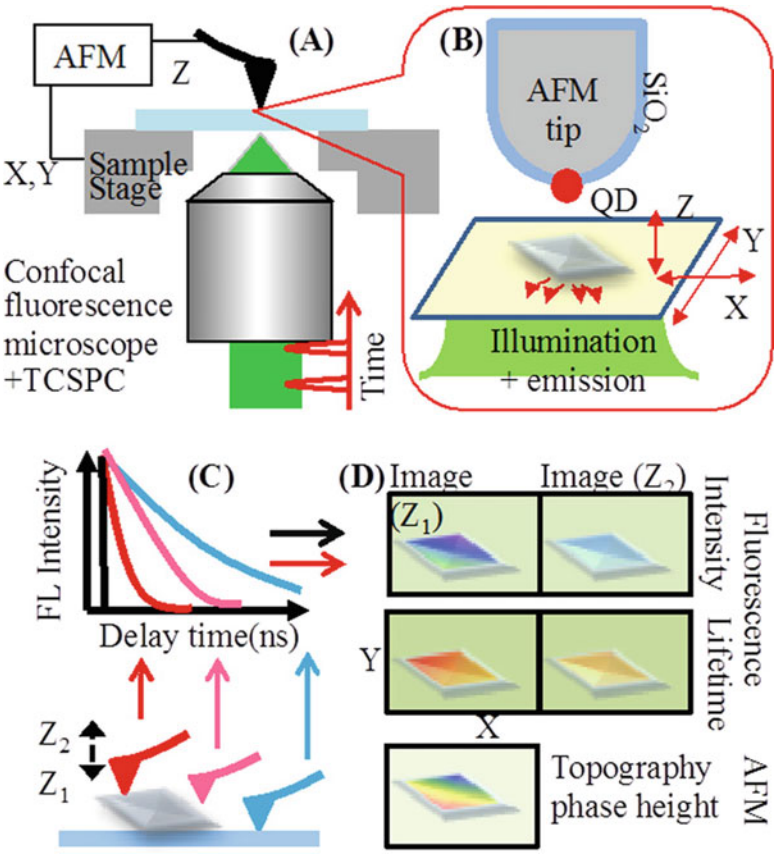

Fig. 2.18 Preparation of single QD-modified AFM tips. (**a**) Procedure for trapping a single QD by a MPTES functionalized AFM tip. (bi) Fluorescence images, (ci) AFM images, and (di) AFM line scan (along the line connecting QDs **a** and **b**) of a 3.5 μm × 3.5 μm area before ($i = 1$) and after ($i = 2$) the attachment of QD **b** to the AFM tip. Inset in c1 and c2 shows an expanded view of QD **b**. (Reprinted with the permission from Ref. [37]. Copyright 2011 American Chemical Society)

coated with a thin layer of SiO_2 (~10 nm) to reduce the quenching of QD emission by the AFM tips. The single QD-modified AFM tip is scanned over the TiO_2 to acquire AFM images, during which the XY positions are controlled by the sample stage and the Z by the AFM tip. The tip is illuminated by laser pulses at 400 nm and the resulting fluorescence is obtained. For every detected photon, the tip position and photon information are recorded using AFM and a time-correlated single-photon counting (TCSPC) board, respectively. The images of fluorescence lifetimes and intensities can be constructed, which can be correlated with the AFM topography/phase images (Fig. 2.18d).

During the measurement, the tip was brought to contact with sample (glass surface or TiO_2) in contact mode. After withdrawing the tip and moving the sample stage laterally, the tip was brought to contact with the next position (Fig. 2.19 a),

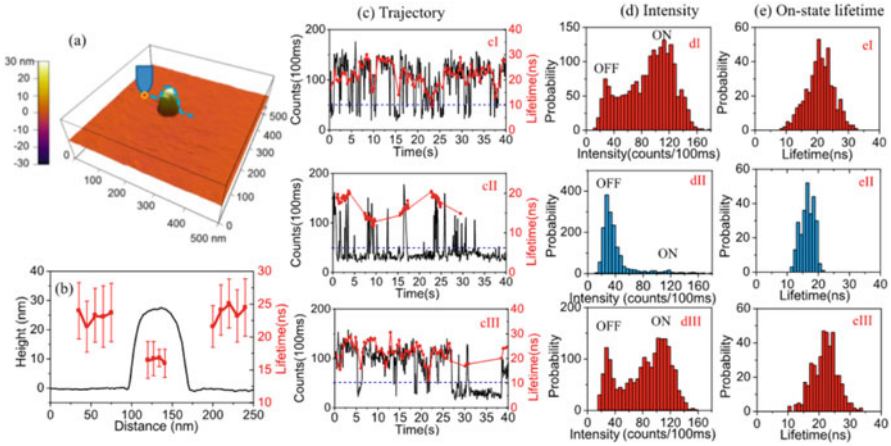

Fig. 2.19 Spatial dependence of electron transfer dynamics from a single QD (attached on a AFM tip) to a TiO_2 nanoparticle. (**a**) The 3D AFM image of a Degussa P25 TiO_2 nanoparticle acquired with a single QD-modified AFM tip operating in ac mode. (**b**) Cross-section line scan of AFM height (black solid line) and average QD on-state emission lifetimes at selected tip−sample contact positions (red circles) along the blue dashed line indicated in panel (**a**). (ci) Typical fluorescence intensity (black) and lifetime (red) trajectories, (di) histograms of intensity distribution, and (ei) histograms of on-state lifetime distribution of a QD-modified AFM tip at the left side (i = I), on top (i = II), and at right side (i = III) of the TiO_2 nanoparticle. The tip is in contact with the glass coverslip in region I and III and with the TiO_2 nanoparticle in region II. Blue dashed lines in cI-III indicate the fluorescence intensity threshold separating the on and off states. (Reprinted with the permission from Ref. [37]. Copyright 2011 American Chemical Society)

presenting the AFM height and the fluorescence information simultaneously (Fig. 2.19b). Representative fluorescence lifetime and intensity trajectories for regions at the left side (i = I), on top (i = II), and at right side (i = III) of the TiO_2 nanoparticle indicate the probability of dark states in region II is higher than regions I and III (Fig. 2.19cI − cIII), respectively. The corresponding intensity distribution histograms (Fig. 2.19dI − III) for points in regions I and III are similar, showing peaks of off and on states at 250 and 1100 counts per second. In comparison, in region II, the probability of on states is much smaller and the off state dominates. It is clear that the probability density of long on states decreases and the probability density of long off states increases in region II compared to regions I and III. Correspondingly, the on-state lifetimes are similar in regions I and III and are significantly shortened in region II (Fig. 2.19eI − III). This finding suggests the feasibility of using electron donor or acceptor modified AFM tips for simultaneous high-resolution imaging of morphology and photoinduced charge-transfer dynamics in nanomaterials.

2.5 In Situ NMR and ESR

The detailed structure−activity relationship of surface hydroxyl groups and adsorbed water on the surface of semiconductor is the key to clarifying the hole-transfer mechanism for photocatalytic water splitting. Owing to the lack of direct experimental evidence, the most controversial point concerning the nature of surface-active sites is whether the surface hydroxyl groups (Ti − OH) of TiO_2 can trap the photogenerated hole. Using the photocatalytic water splitting by Pt/TiO_2 as an example, one- (1D) and two-dimensional (2D) ^1H solid-state NMR together with in situ ESR techniques were employed to identify surface hydroxyl groups and adsorbed water molecules, as well as their spatial proximity/interaction on the surface of TiO_2 [38].

Two different types of Ti−OH including bridging hydroxyl (OH_B, 7.3 ppm) and terminal hydroxyl (OH_T, 1.8 ppm) groups were identified from 1D NMR spectroscopy (Fig. 2.20). 2D $^1H-^1H$ double-quantum (DQ) MAS NMR spectroscopy presents autocorrelation peaks along the diagonal (ω, 2ω) resulting from the dipolar interaction of protons with the same chemical shift spectroscopy, which can probe the spatial proximities of various Ti−OH groups and the adsorbed H_2O. The 2D $^1H-^1H$ DQ MAS NMR spectrum of Pt/TiO_2 dehydrated at 673 K shows only one diagonal peak at (1.8, 3.6) ppm due to the autocorrelation of OH_T groups, indicating that they are in close spatial proximity to each other. The presence of 0.9 μmol H_2O results in two diagonal peaks at (1.8, 3.6) and (7.3, 14.6) ppm, corresponding to the autocorrelations of OH_T and OH_B groups, respectively. The more introduction of H_2O resulted in new peaks. The new autocorrelation peak at (5.2, 10.4) ppm was ascribed to the spatial proximity of the hydrogen atom of adsorbed H_2O. Another

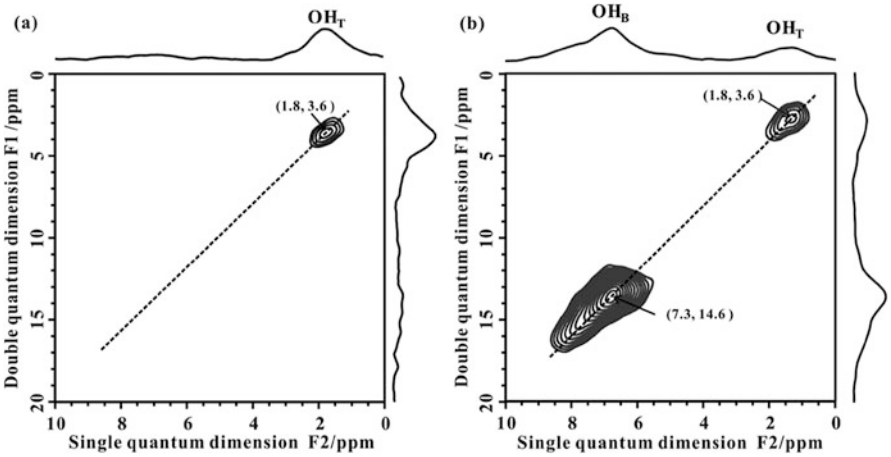

Fig. 2.20 2D $^1H-^1H$ DQ MAS NMR spectra of (**a**) bare PT-2 and (**b**) PT-2 loaded with H_2O (0.9 μmol). (Reprinted with the permission from Ref. [38]. Copyright 2011 American Chemical Society)

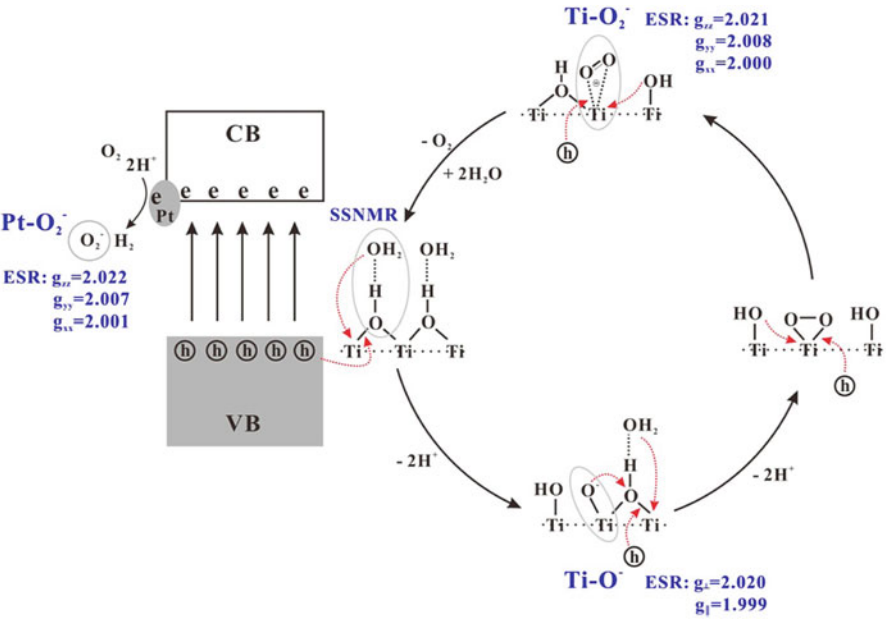

Scheme 2.1 Proposed hole-transfer mechanism for photocatalytic water splitting on the TiO_2 photocatalyst upon solar light irradiation. (Reprinted with the permission from Ref. [38]. Copyright 2011 American Chemical Society)

new autocorrelation peak appeared at (6.9, 13.8) ppm, and it grew with the consumption of the autocorrelation peak at (7.3, 14.6) ppm when the H_2O loading was gradually increased. The signal at 6.9 ppm was assigned to the ^1H signal of OH_B in hydrogen-bonding interaction with surface-adsorbed H_2O. Besides the autocorrelation peaks, the intense off-diagonal peak pair at (5.2, 12.1) and (6.9, 12.1) ppm correspond to the spatial correlation between H_2O and OH_B. All these findings demonstrated that H_2O only adsorbs on OH_B groups through hydrogen-bonding interaction, forming hydrated OH_B groups.

The in situ ^1H and ^{13}C NMR studies of the photocatalytic reaction on TiO_2 with different Ti−OH groups and different H_2O loadings illustrated that the enhanced activity was closely correlated to the amount of hydrated OH_B groups. The in situ ESR experiments performed with variable H_2O loading revealed that the hydrated OH_B offer a channel for the transfer of photogenerated holes in the photocatalytic reaction, and the adsorbed H_2O has a synergistic effect with the neighboring OH_B group to facilitate the formation and evolution of active paramagnetic intermediates. As shown in Scheme 2.1, upon the solar light irradiation, the hydrated OH_B groups trap a photoinduced hole to generate the Ti−O^- intermediate. Meanwhile, a nucleophilic attack of adsorbed H_2O to the hole-trapped sites occurs, which hinders the recombination of photoinduced electrons and holes, and thereby stabilizes the formation of Ti−O^- species. When another photoinduced hole is trapped by a neighboring hydrated OH_B group and the hole-trapped site is nucleophilically

attacked by another adsorbed H_2O, two adjacent $Ti - O^-$ centers can couple with each other to form surface peroxide species. The surface peroxide intermediate would be oxidized by photoinduced holes to form $Ti{-}O_2^-$ species, which can be further oxidized by the photoinduced hole, forming an O_2 molecule followed by the recovery of OH_B group. The excessive H_2O molecules adsorb on the regenerated OH_B groups, which may hinder the interaction between the O_2 molecule and the TiO_2 surface and further prevent the O_2 molecule from trapping the photoinduced electron to form $Ti{-}O_2^-$ species. Then the O_2 molecule would interact with the cocatalyst Pt and be reduced to form $Pt{-}O_2^-$ species by the photoinduced electron. The reduction of O_2^- species by the photoinduced electron ($O_2^- + 2H^+ + e \rightarrow H_2O_2 + 2H^+ + 2e \rightarrow 2H_2O$) should be responsible for the low efficiency of the photocatalytic water splitting. Meanwhile, the reduction of H^+ from the above recycle by photoinduced electrons on the cocatalyst Pt produces the H_2 molecule.

References

1. Nosaka Y, Nosaka AY (2017) Generation and detection of reactive oxygen species in photocatalysis. Chem Rev 117:11302–11336
2. Hirakawa T, Nosaka Y (2008) Selective production of superoxide ions and hydrogen peroxide over nitrogen- and sulfur-doped TiO_2 photocatalysts with visible light in aqueous suspension systems. J Phys Chem C 112:15818–15823
3. Wang D, Zhao L, Guo LH et al (2014) Online detection of reactive oxygen species in ultraviolet (UV)-irradiated nano-TiO_2 suspensions by continuous flow chemiluminescence. Anal Chem 86:10535–10539
4. Kakuma Y, Nosaka AY, Nosaka Y (2015) Difference in TiO_2 photocatalytic mechanism between rutile and anatase studied by the detection of active oxygen and surface species in water. Phys Chem Chem Phys 17:18691–18698
5. Ishibashi K, Fujishima A, Watanabe T et al (2000) Hashimoto, K. Generation and deactivation processes of superoxide formed on TiO_2 film illuminated by very weak UV light in air or water. J Phys Chem B 104:4934–4938
6. Dimitrijevic NM, Rozhkova E, Rajh T (2009) Dynamics of localized charges in dopamine-modified TiO_2 and their effect on the formation of reactive oxygen species. J Am Chem Soc 131:2893–2899
7. Tachikawa T, Majima T et al (2010) Single-molecule, single-particle fluorescence imaging of TiO_2-based photocatalytic reactions. Chem Soc Rev 39:4802–4819
8. Naito K, Tachikawa T, Fujitsuka M et al (2008) Real-time single-molecule imaging of the spatial and temporal distribution of reactive oxygen species with fluorescent probes: applications to TiO_2 photocatalysts. J Phys Chem C 112:1048–1059
9. Xu W, Jain PK, Beberwyck BJ et al (2012) Probing redox photocatalysis of trapped electrons and holes on single Sb-doped titania nanorod surfaces. J Am Chem Soc 134:3946–3949
10. Kim W, Tachikawa T, Moon G et al (2014) Molecular-level understanding of the photocatalytic activity difference between anatase and rutile nanoparticles. Angew Chem Int Ed 53:14036–14041
11. Tachikawa T, Wang N, Yamashita S et al (2010) Design of a highly sensitive fluorescent probe for interfacial electron transfer on a TiO_2 surface. Angew Chem Int Ed 49:8593–8597
12. Tachikawa T, Yamashita S, Majima T (2011) Evidence for crystal-face-dependent TiO_2 photocatalysis from single-molecule imaging and kinetic analysis. J Am Chem Soc 133:7197–7204

13. Ha JW, Purnima T, Ruberu A et al (2014) Super-resolution mapping of photogenerated electron and hole separation in single metal−semiconductor manocatalysts. J Am Chem Soc 136:1398–1408
14. Tachikawa T, Yamashita S, Majima T (2010) Probing photocatalytic active sites on a single titanosilicate zeolite with a redox-responsive fluorescent dye. Angew Chem Int Ed 49:432–435
15. Naito KT, Tachikawa T, Fujitsuka M et al (2009) Single-molecule observation of photocatalytic reaction in TiO_2 nanotube: importance of molecular transport through porous structures. J Am Chem Soc 131:934–936
16. Szczepankiewicz SH, Colussi AJ, Hoffmann MR et al (2000) Infrared spectra of photoinduced species on hydroxylated titania surfaces. J Phys Chem B 104:9842–9850
17. Nakamura R, Imanishi A, Murakoshi K et al (2003) In situ FTIR studies of primary intermediates of photocatalytic reactions on nanocrystalline TiO_2 films in contact with aqueous solutions. J Am Chem Soc 125:7443–7450
18. Sato S, Ueda K, Kawasaki Y et al (2002) In situ IR observation of surface species during the photocatalytic decomposition of acetic acid over TiO_2 films. J Phys Chem B 106:9054–9058
19. Nakamura R, Nakato Y (2004) Primary intermediates of oxygen photoevolution reaction on TiO_2 (rutile) particles, revealed by in situ FTIR absorption and photoluminescence measurements. J Am Chem Soc 126:1290–1298
20. Sivasankar N, Weare WW, Frei H (2011) Direct observation of a hydroperoxide surface intermediate upon visible light-driven water oxidation at an Ir oxide nanocluster catalyst by rapid-scan FT-IR spectroscopy. J Am Chem Soc 133:12976–12979
21. Zhang M, Respinis MD, Frei H (2014) Time-resolved observations of water oxidation intermediates on a cobalt oxide nanoparticle catalyst. Nat Chem 6:362–367
22. Zandi O, Hamann TW (2016) Determination of photoelectrochemical water oxidation intermediates on haematite electrode surfaces using operando infrared spectroscopy. Nat Chem 8:778–783
23. Krishnan RS, Shankar RK (1981) Raman effect: history of the discovery. J Raman Spectrosc 10:1–8
24. McCreery RL (2000) Raman spectroscopy for chemical analysis. Wiley, New York
25. Nie SM, Emory SR (1997) Probing single molecules and single nanoparticles by surface-enhanced Raman scattering. Science 275:1102–1106
26. Huang Y, Zhang M, Zhao L et al (2014) Activation of oxygen on gold and silver nanoparticles assisted by surface plasmon resonances. Angew Chem Int Ed 53:2353–2357
27. Yan YF, Wang LZ, Tan XJ et al (2016) Surface-enhanced Raman spectroscopy assisted by radical capturer for tracking of plasmon-driven redox reaction. Sci Rep 6:30193
28. Wang J, Ando RA, Camargo PHC (2015) Controlling the selectivity of the surface plasmon resonance mediated oxidation of p-aminothiophenol on Au nanoparticles by charge transfer from UV-excited TiO_2. Angew Chem Int Ed 54:6909–6912
29. Qi D, Yan X, Wang L et al (2015) Plasmon-free SERS self-monitoring of catalysis reaction on Au nanoclusters/TiO_2 photonic microarray. Chem Commun 51:8813–8816
30. Tan X, Wang L, Cheng C et al (2016) Plasmonic MoO_{3-x}@MoO_3 nanosheets for highly sensitive SERS detection through nanoshell-isolated electromagnetic enhancement. Chem Commun 52:2893–2896
31. Alessandri I (2013) Enhancing Raman scattering without plasmons: unprecedented sensitivity achieved by TiO_2 Shell-based resonators. J Am Chem Soc 135:5541–5544
32. Qi D, Lu L, Wang L et al (2014) Improved SERS sensitivity on plasmon-free TiO_2 photonic microarray by enhancing light-matter coupling. J Am Chem Soc 136:9886–9889
33. Xing YL, Yan R, Lo S et al (2014) Alumina-coated Ag nanocrystal monolayers as surface-enhanced Raman spectroscopy platforms for the direct spectroscopic detection of water splitting reaction intermediates. Nano Res 7:132–143
34. Yan XF, Xu Y, Tian BZ et al (2017) Operando SERS self-monitoring photocatalytic oxidation of aminophenol on TiO_2 semiconductor. Appl Catal B: Environ. https://doi.org/10.1016/j.apcatb.2017.10.009

35. Sevinc PC, Wang X, Wang Y et al (2011) Simultaneous spectroscopic and topographic near-field imaging of TiO_2 single surface states and interfacial electronic coupling. Nano Lett 11:1490–1494
36. He Y, Rao G, Cao J et al (2016) Simultaneous spectroscopic and topographic imaging of single-molecule interfacial electron-transfer reactivity and local nanoscale environment. J Phys Chem Lett 7:2221–2227
37. Liu Z, Zhu H, Song N et al (2013) Probing spatially dependent photoinduced charge transfer dynamics to TiO_2 nanoparticles using single quantum dot modified atomic force microscopy tips. Nano Lett 13:5563–5569
38. Liu F, Feng N, Wang Q et al (2017) Transfer channel of photoinduced holes on a TiO_2 surface as revealed by solid-state nuclear magnetic resonance and electron spin resonance spectroscopy. J Am Chem Soc 139:10020–10028